

The Braking Behaviors of Cu-Based Metallic Brake Pad for High-Speed Train Under Different Initial Braking Speed

Tao Peng¹ · Qingzhi Yan¹ · Gen Li¹ · Xiaolu Zhang¹ · Zefeng Wen² · Xuesong Jin²

Received: 20 March 2017 / Accepted: 22 August 2017 / Published online: 6 September 2017
© Springer Science+Business Media, LLC 2017

Abstract The purpose of this research was to study the braking behaviors of Cu-based composite pad under real operating conditions of high-speed train. A series of pad-on-disk braking tests was performed with the initial braking speed (IBS) from 80 to 380 km/h. Results showed that the coefficient of friction (COF) of the brake pad demonstrated a three-stage feature with the increase in IBS. It decreased from 0.395 to 0.358 with the increase in IBS from 80 to 200 km/h, then increased to 0.398 when IBS reached 320 km/h; and fell again to 0.379 at 380 km/h. Similarly, the pad also displayed three wear regimes as IBS increased, i.e., (1) mild wear (80–160 km/h), (2) moderate wear (200–250 km/h), and (3) severe wear (300–380 km/h). Surface morphologies and phase analyses indicate that the evolution of the COF mainly depends upon the state of friction film. The formation or completion of friction film regularly contributes to a lower COF and wear rate, while the destruction of friction film results in a higher COF and wear rate. Besides, the “lubricants” induced by high braking temperature are also responsible for the change in the COF. As IBS increased, the key wear mechanisms changed from abrasion, plowing, and oxidation to delamination at 250 km/h.

Keywords Braking behaviors · Metallic brake pad · High-speed train · Inertia braking tests

1 Introduction

An ideal brake pad for trains with a suitable and stable coefficient of friction (COF) and low wear rate irrespective of temperature, humidity, and corrosion is desired by researchers and engineers [1, 2]. However, due to the nature that material properties change in environment and complex operating conditions, no perfect materials have been found in the brake pad for trains. Generally speaking, there are three generations of materials that have been used as brake pad for trains. Synthetic resin was common in early ages which can only be used in low speed. Once the higher temperature caused by higher braking speed is introduced into the braking system, deterioration of properties of resin is inevitable [3]. Then, metallic composite brake pads prepared by powder metallurgy (P/M) emerged as a promising material with good thermal resistance, ductility, and suitable cost [4, 5]. Further, ceramic or ceramic composite, like carbon-reinforced silicon carbide, was introduced as future pad material [6, 7] for lightweight and enhanced wear resistance. However, the high cost and long preparing period, as well as the unstable COF under the low speed [8], make it a long way before commercial application. Right now, the third generation of pad material has only been used for scientific research [9–11]. Hence, metallic brake pad is still widely used for trains at present in China.

Though metallic pads demonstrate a suitable combination of hardness, strength, and ductility, evolutive operating conditions for trains, especially for high-speed trains, are new and great challenges for metallic pads. Due to the

✉ Qingzhi Yan
qzyan@ustb.edu.cn

¹ Laboratory of Special Ceramics and Powder Metallurgy, University of Science and Technology Beijing, Beijing 100083, China

² Tribology Research Institute, State Key Laboratory of Traction Power, Southwest Jiaotong University, Chengdu 610031, China

greatly improved running speed (up to 380 km/h), an unprecedented amount of energy and temperature has been introduced into the brake system, and a series of problems, including matrix softening and fading have been surfaced. Despite the complexity of brake material testing that has evolved over the years, the braking behaviors and properties of metallic pads under extensive velocity ranges are still a lack of essential knowledge due to the lack of enough accumulation of research under high speed. Currently, most of the researches on brake pads for trains are conducted under mild sliding conditions (lower applied load or lower sliding speed or lower rotary inertia) [4, 12].

In this work, systematic braking tests simulated in real operating conditions of high-speed train from 80 to 380 km/h were conducted on a subscale inertia-type braking dynamometer to investigate the braking behaviors of a typical commercial brake pad material sliding against a forged steel disk under controlled laboratory conditions. Detailed observations of friction surface and related tests were made trying to further elucidate the changes during the braking.

2 Experiments

2.1 Sample

The metallic braking pad used in this investigation was a commercial brake pad designed for high-speed train applications in China, which combines up to 8 ingredients, such as Cu, Fe, graphite, Cr, ferrochrome alloy (Cr–Fe), MoS₂, SiO₂, Al₂O₃, and the corresponding element compositions are listed in Table 1. The macro-photograph and the backscattered electron image (BSE) of starting brake pad are shown Fig. 1, in which some of the components are indicated by arrows based on the energy-dispersive X-ray spectrometry (EDS) identification. Note that flake graphite, Cr–Fe, SiO₂, and Al₂O₃ preserved the original powder appearances. The nominal friction area of the braking pad was 1700 mm². A forged steel rotor disk (30CrSiMoVA) with a diameter of 450 mm and a thickness of 35 mm was used as a counterpart, which is widely assembled in current high-speed train in China.

2.2 Braking Tests

The braking tests were conducted on a single-ended inertial-type braking dynamometer (TM-I, China. Fig. 2),

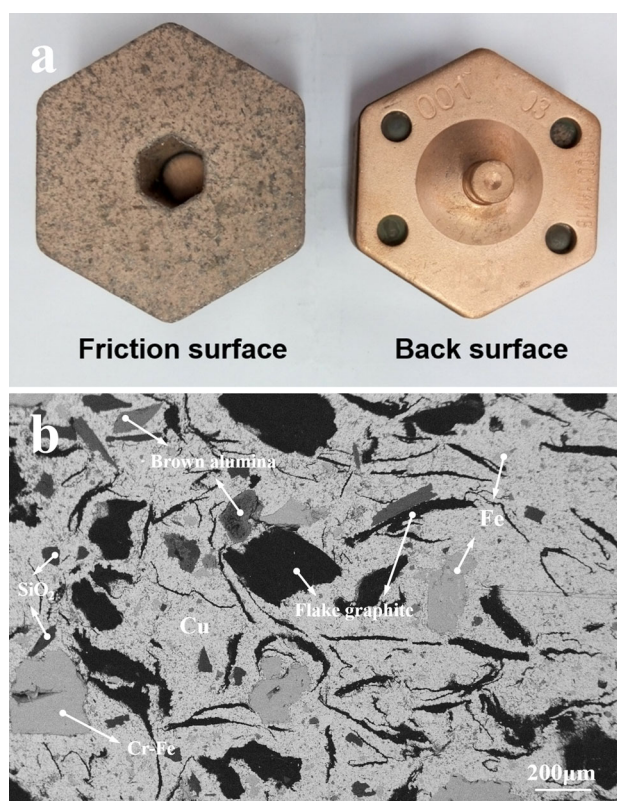


Fig. 1 a Macro-photograph and b backscattered electron image (BSE) of starting brake pad

designed to reproduce the full-scale thermal mechanical loading at the laboratory subscale. The scaling approach is based on a scale conversion rule [13], and the main characteristics of the tester are listed in Table 2.

Experimental conditions correspond to nine emergency stop brakings for high-speed trains running at 80, 120, 160, 200, 250, 300, 320, 350, and 380 km/h. In all cases, the full-scale stop-braking duration was satisfied, while the initial braking speed (IBS), the brake inertia, and the mean contact pressure were chosen in conformity with the scale conversion rule. The brake inertia was set as 19.4 kg m² corresponding to 12.3 tons of mass to be stopped per disk in the real train, and the normal pressure was 1.1 MPa.

Braking test was performed by accelerating the rotation shaft with the steel counterpart disk to the desired working speed. When the speed was reached, motor power was switched off, and two fixed metallic pads were simultaneously pressed against the steel counterpart at a desired normal pressure and a mean friction radius of 125 mm until the rotation shaft completely stopped. During each test, the relevant parameters were as follows:

Table 1 Compositions of the P/M pad

Elements	Cu	Fe	Cr	Si	Al	Mo	S	C	O	Na	Ca	Mg
Mass (wt.%)	44.7	33.2	5.6	1.5	0.56	1.36	1.02	11.3	0.5	0.03	0.05	0.02

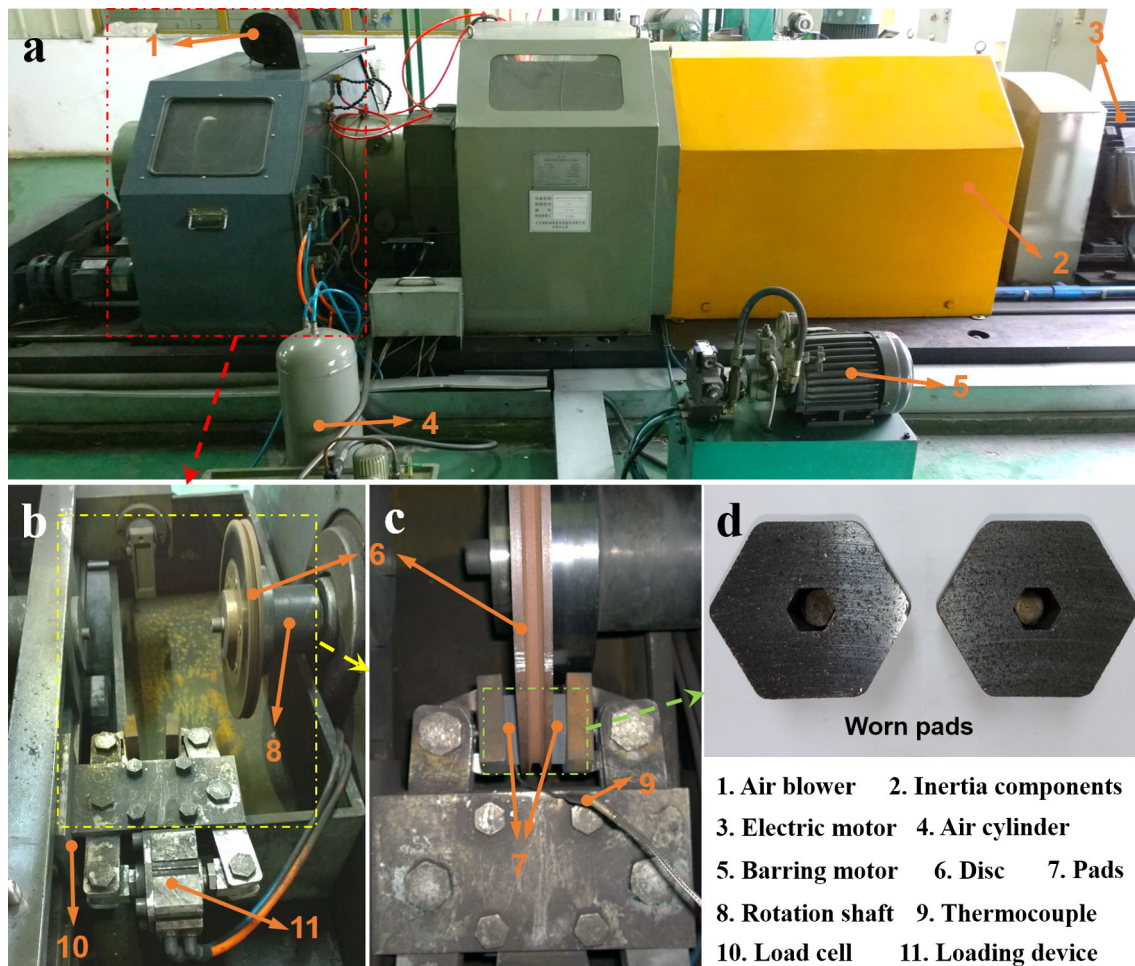


Fig. 2 Schematic diagram of the subscale brake material testing dynamometer. **a** External diagram, **b** inside diagram, **c** pad-on-disk configuration, **d** worn pads

Table 2 Subscale testing dynamometer: main characteristics

Electric motor power	80 kW
Rotation speed	up to 4500 rpm
Normal load	up to 4.8 kN
Simulated inertia range	[12–47] kg m ²
Sliding velocity	up to 70 m s ⁻¹
Dissipated energy	up to 2.5 MJ

- The transient COF and mean COF were automatically calculated by the computer system based on the measured friction torque and imposed force.
- Pad subsurface temperature was measured by a thermocouple located 2 mm beneath the contact surface within the pad.
- Pad wear was measured by checking its weight, M , before and after each test using an analytical balance (D&T ES5000, with an accuracy of 0.01 g). Data were

then converted into wear volumes, V , using the measured density of the pad. The specific wear rate, W_r , was determined from wear volumes normalized by dissipated energy, E_s , using Eq. (1):

$$W_r = V/E_s \quad (1)$$

Before each test, we conducted seven times run-in brakes to ensure a favorable contacting surface between the pad and disk. To ensuring the reliability of the experiment's data, the braking test at each IBS was repeated three times, and the mean value of three is reported in this work.

2.3 Characterization Methods

Physical properties and mechanical properties of the braking pad, including density, porosity, hardness, shear strength, and compressive strength, were tested according to China Railways Production Certification Center standards (CRCC). The density and porosity were tested via

Archimedes' principle. The Brinell hardness of the initial pad was tested on the HB-3000 hardness tester (China) in accordance with GB/T 231.1-2009. The strength was measured on the WDW-200 W universal testing machine (China) based on GB/T 6525-1986. The thermal properties were measured by the Laserflash thermal analyzer (NETZSCH, LFA-427, Germany).

Field emission scanning electronic microscope (FESEM, FEI Quanta 450, USA) attached with electron diffraction spectroscopy (EDS) was applied to examine the surface and vertical section morphologies of the worn pads as well as the wear debris after the braking tests.

3 Results and Discussion

3.1 Mechanical Properties of Braking Pad

Table 3 shows the physical properties and mechanical properties, including density, porosity, hardness, strength, and thermal conductivity of braking pad in this investigation. It can be seen that the pad presented suitable strength with rather soft matrix, which met the requirements of TB/T 3470-2016.

3.2 Friction Behaviors

As is known, the emergency stop-braking is a decelerating motion with a constant pressure until a stop is achieved. Three typical instantaneous COF curves represented different IBS in the tests are shown in Fig. 3. The instantaneous COF was relatively constant during a single brake stop in 380 km/h, while they increased gradually at the end of a stop in 80 and 200 km/h cases, which was commonly called anti-fade.

Figure 4 demonstrates the mean COFs and maximum subsurface temperatures (T_{\max}) versus IBS curves at the same pressure and inertia. The COF curve shows a three-stage feature with the increase in IBS from 80 to 380 km/h in the investigation. At the low-speed stage (80–200 km/h), the COF decreased from 0.395 to 0.358 with increasing IBS. At the medium-speed stage (250–320 km/h), the COF increased with IBS and reached a maximum value of 0.398 at 320 km/h. Finally, at the high-speed stage (350–380 km/h), it fell to 0.379 with increasing IBS. Note that the

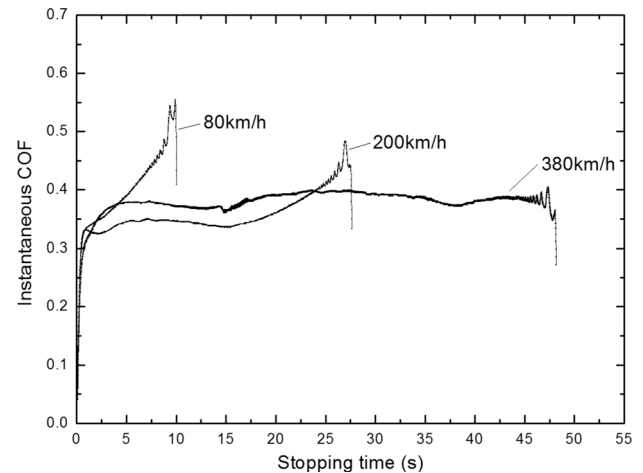


Fig. 3 Typical instantaneous coefficient of friction (COF) curves in the emergency stop-braking tests

fluctuation of the COFs at different IBS is less than 15% (meet the requirements of CRCC). The three-stage curve suggests that the key factor that influenced the friction and wear behaviors may vary at different stage. Meanwhile, the T_{\max} firstly increased from 120 to 626 °C with the increase in IBS from 80 to 350 km/h and then dropped to 610 °C at 380 km/h, which implies some particular change of the pad at the highest speed.

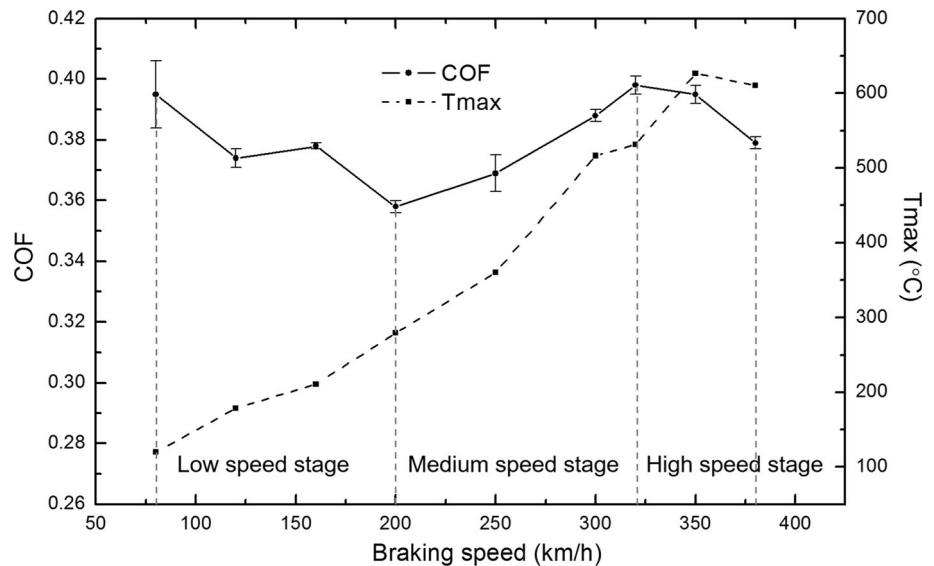
In order to explore the change in the mean COFs, the friction surfaces of braking pad after each stop-braking were examined by FESEM. Although the “postmortem” observation cannot exactly reflect what is going on during one braking process, it also contains much useful information left behind after one stop, like damage accumulation on surface, coverage of friction film, local melting.

Figure 5 presents the microstructure of friction surfaces at the low-speed stage. At 80 km/h, many graphite particles (black strips) and hard particles (black granules) remained visible on the surface, and numerous loose third body particles (light-gray contrast) were trapped in the hollow of the friction surface (Fig. 5a). It is known that the compaction and interaction of third body particles are a prerequisite to form the friction film (or “compacted plane”), and the formed friction film always plays an important role in the friction process [14–16]. Backscattered electron (BSE) images thereby were used to distinguish the friction film from the other areas due to atomic number contrast

Table 3 Partial properties of braking pad

Density (g/cm ³)	Porosity (%)	Hardness (HB)	Shear strength (MPa)	Compressive strength (MPa)	Thermal conductivity (30 °C) (W m ⁻¹ K ⁻¹)
4.9	21.1	13.5	11	110	17.35

Fig. 4 Mean COFs and maximum subsurface temperatures (T_{\max}) at different initial braking speed (IBS)



differences (Fig. 5e–h). At 80 km/h, only a few patchy friction film (dark-gray contrast) was formed on the surface (Fig. 5e), as the EDS identification revealed that the friction film (marked “1”) was mainly composed of copper or iron oxides, while the area in white contrast (marked “2”) was approximately metallic constituent (Table 4). As IBS increased, the third body particles mixed and gradually compacted to bury the exposed graphite and hard particles and to form a continuous friction film. As IBS exceeded 160 km/h, both secondary electron (SE) images and BSE images suggest that the friction surface was covered by a nearly complete and continuous friction film (Fig. 5c–d, g–h). What is more, it seems that the friction surface was partly recovered by a recompacted layer at 200 km/h, and the compositions of this layer (marked “3” in Fig. 5h) was similar with that of the friction film (marked “1”) in 80 km/h (Table 4).

Different from the morphological features at the low-speed stage, at 250–320 km/h, the SE images demonstrate that some pits began to appear on the friction surfaces (Fig. 6). Meanwhile, more and more graphite particles and metallic constituents (white regions in Fig. 6d–f), which had been coated with compacted third bodies, resurfaced and were in sliding contact with mating steel due to the wear of the friction film. What is more, some Cr–Fe particles were also exposed on the surface. These features indicate that the friction film started to rupture at the medium-speed stage.

In addition, the vertical section profile (Fig. 7) demonstrates another feature in this stage. A Cr–Fe particle emerged on the surface and was broken into pieces, which may be caused by the drastic collision between the interlock asperities of the contact pairs (Fig. 7a). And the other image revealed those fragments may then be mixed up with

the third body particles and further crushed into the friction film (Fig. 7b).

Finally, when IBS increased to the high-speed stage (Fig. 8), the size of pits expanded a lot, and the friction surface herewith developed into some discrete contact plateaus. Such phenomena imply that the material may be easily removed from the tribological system in this stage. What is more, inhomogeneous regions marked with different contrast, as shown in BSE images (Fig. 8c, d), demonstrate that the friction films were broken seriously. The real contact area may be decreased due to the ruin of the contact plateau.

What is more, we also found a peculiar phenomenon at the highest speed. As shown in Fig. 9a, there are lots of pot holes on the contact surface at 380 km/h, which has not been observed at any lower IBS. We hypothesize that these pot holes may be resulted from local melting of some low-melting-point phases, because the flash temperatures generated on local hot spot could exceed 1000 °C [17, 18], which is close to the melting point of Cu matrix. The element area profile revealed that these pot holes only could be observed in the Cu-rich areas (Fig. 9b). This means that Cu was likely to be partly melted, and there may be a liquid film formed on the contact surface during the friction process.

On the other hand, the representative vertical section microstructures, as shown in Fig. 10, visually displays the evolution of subsurface at different stage. Note that there was only a little film covering on the surface at 80 km/h (Fig. 10a). When IBS increased to 200 km/h, a complete friction film was formed on the surface with the thickness of about 20 μm (Fig. 10b). At 320 km/h, the friction film was destroyed a lot. Besides, Cr–Fe particle was broken into pieces, and some cracks were already formed at a

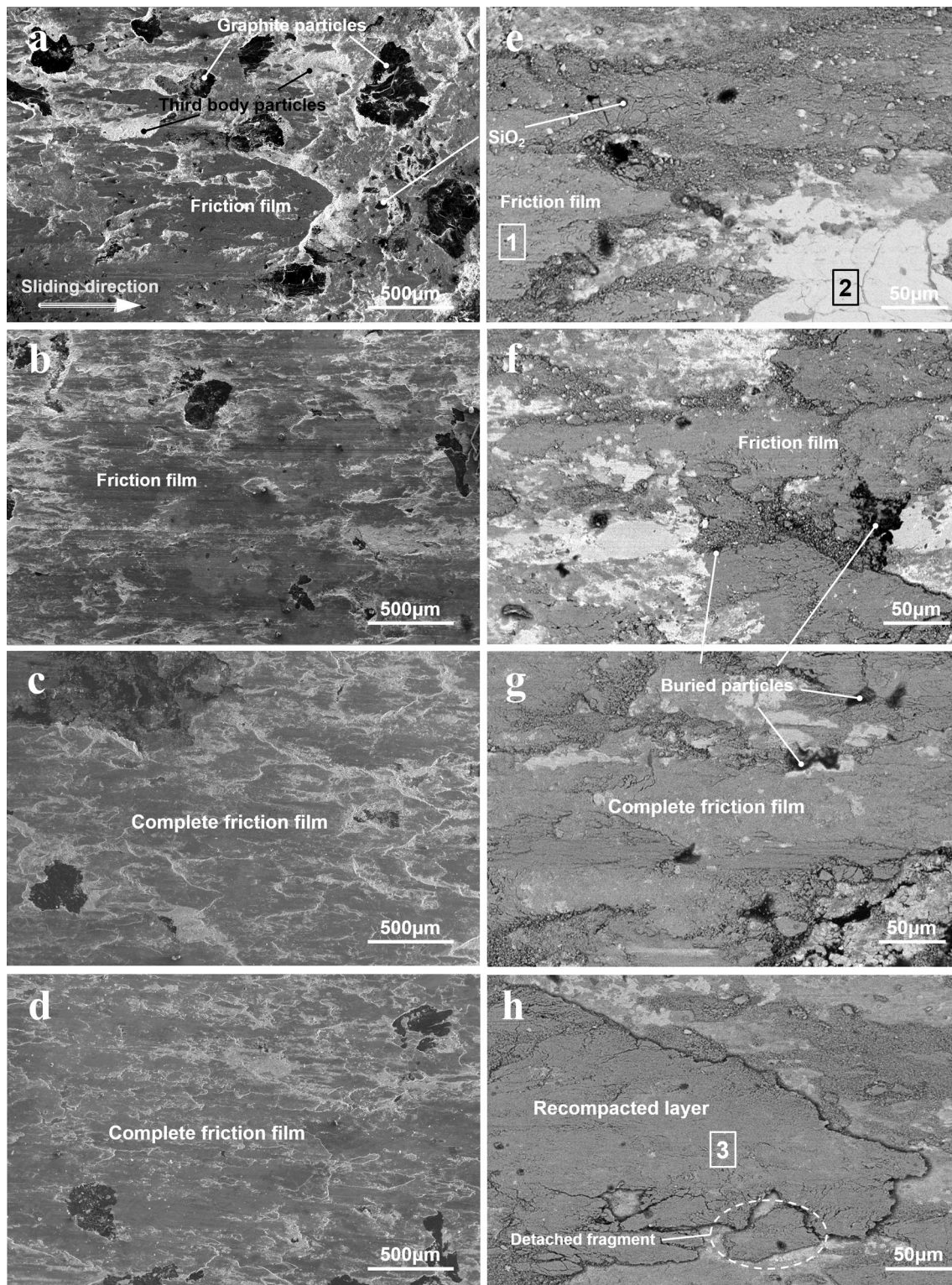


Fig. 5 Surface morphologies at the low-speed stage. SE images: **a** 80 km/h, **b** 120 km/h, **c** 160 km/h, **d** 200 km/h; BSE images: **e** 80 km/h, **f** 120 km/h, **g** 160 km/h, **h** 200 km/h

certain depth beneath the surface. Finally, the friction film was barely visible when IBS reached 380 km/h, and the contact surface became vulnerable. As shown in Fig. 10d,

numerous cracks preferentially initiated from the interface of graphite/matrix and propagated out the surface, which made peeling easy. The vertical section views indicate that

Table 4 Compositions of different area in Fig. 5 (wt.%) (Carbon was not quantified)

No.	Cu	Fe	O	Cr	Si	Al	Mo	S
1	32.1	45.6	17.2	1.5	1.3	0.3	1.2	0.8
2	60.8	32.3	5.6	0.9	0.1	/	0.1	0.2
3	31.6	42.3	21.6	1.8	1.1	0.5	0.6	0.5

the friction film experienced a formation–completion–destruction process, which was compatible with the evolution of surface morphologies as mentioned above.

To further explore the compositional variation of friction surfaces under different IBS, XRD measurements were used, and the representative patterns are shown in Fig. 11.

At low IBS (80 km/h), the oxide peaks, mainly Cu_2O and FeO , were very feeble, while graphite and SiO_2 peaks can be clearly observed. The locations for main peak of Fe (110) at 2θ of 44.67° and Cr–Fe (110) at 2θ of 44.55° are overlapped and hard to be distinguished from each other in the XRD patterns. As IBS increased to 200 km/h, the intensity of oxide peaks increased. Meanwhile, the intensity of graphite peak decreased to a low level, and SiO_2 peak disappeared. When IBS exceeded 320 km/h, FeO was further oxidized to Fe_3O_4 . Besides, the intensity of graphite peak returned to a high level and SiO_2 peak reappeared.

Combined the surface morphologies with the patterns, it seems that the change in the intensities of graphite and SiO_2 peaks had a close relationship with the formation and

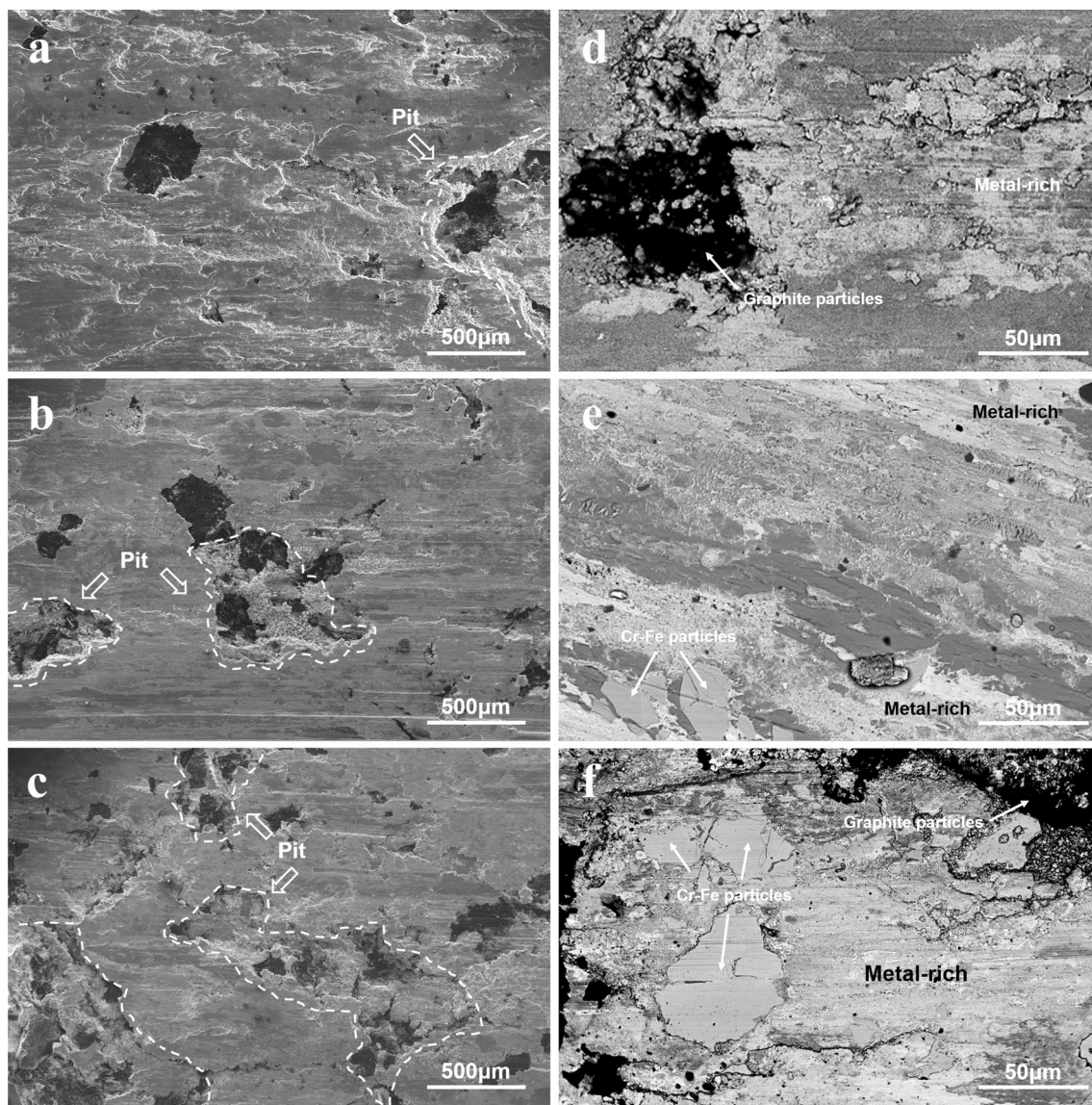


Fig. 6 Surface morphologies at the medium-speed stage. SE images: **a** 250 km/h, **b** 300 km/h, **c** 320 km/h; BSE images: **d** 250 km/h, **e** 300 km/h, **f** 320 km/h

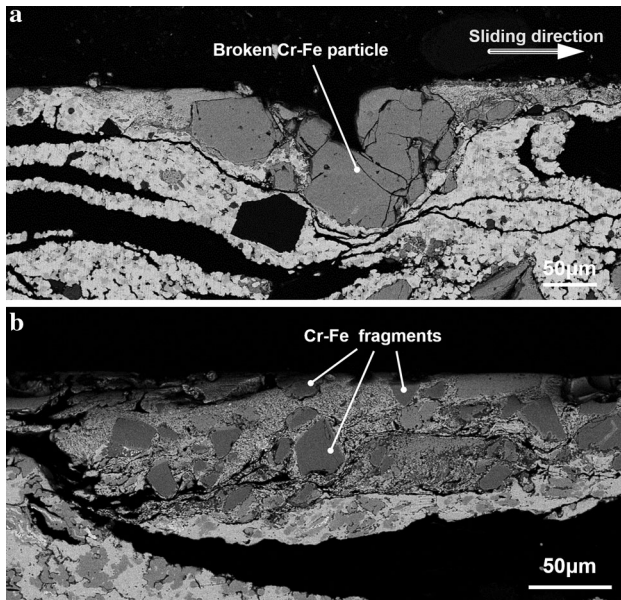


Fig. 7 Typical vertical section profile at the medium-speed stage. **a** Broken Cr-Fe particles, **b** Cr-Fe fragments crushed into the friction film

destruction of the friction film on the surfaces. More precisely, the decrease or disappearance of these peaks may be caused by the coverage of friction film, while the increase or reappearance of them is probably induced by the destruction of the covered film.

Based on the surface morphologies and phase analyses, it can be concluded that during the low-speed stage, since the contact surface was gradually covered by the friction film, “metal-on-metal” contact can be effectively suppressed, and the friction force is diminished consequently. Therefore, the COF decreased with the increase in IBS in this stage. At the medium-speed stage, with the increase in IBS, the friction film was gradually ruptured and “metal-on-metal” contact in local regions was enhanced, leading to greater adhesive shear and increased friction. In addition, the Cr-Fe fragments can be served as “hard asperities” on the contact surface, due to their good chemical stability, high strength, and excellent bonding strength with the matrix (even higher than the matrix itself) [19, 20]. As these “hard asperities” exposed on the surface, friction force originated from the mechanical interlocking was enlarged and the COF herewith increased. At the high-speed stage, the serious peeling of material led to the decrease in the real contact plateau, which also means the decrease in the capacity to dissipate energy, and it may be responsible for the declined COF. On the other hand, the lubricative fluid film induced by melting Cu may be another reason for the decrease in COF at 380 km/h. Besides, the liquid film can not only decrease the drag force between the friction pair, but also significantly reduces the temperature of contact surface [21], and it can

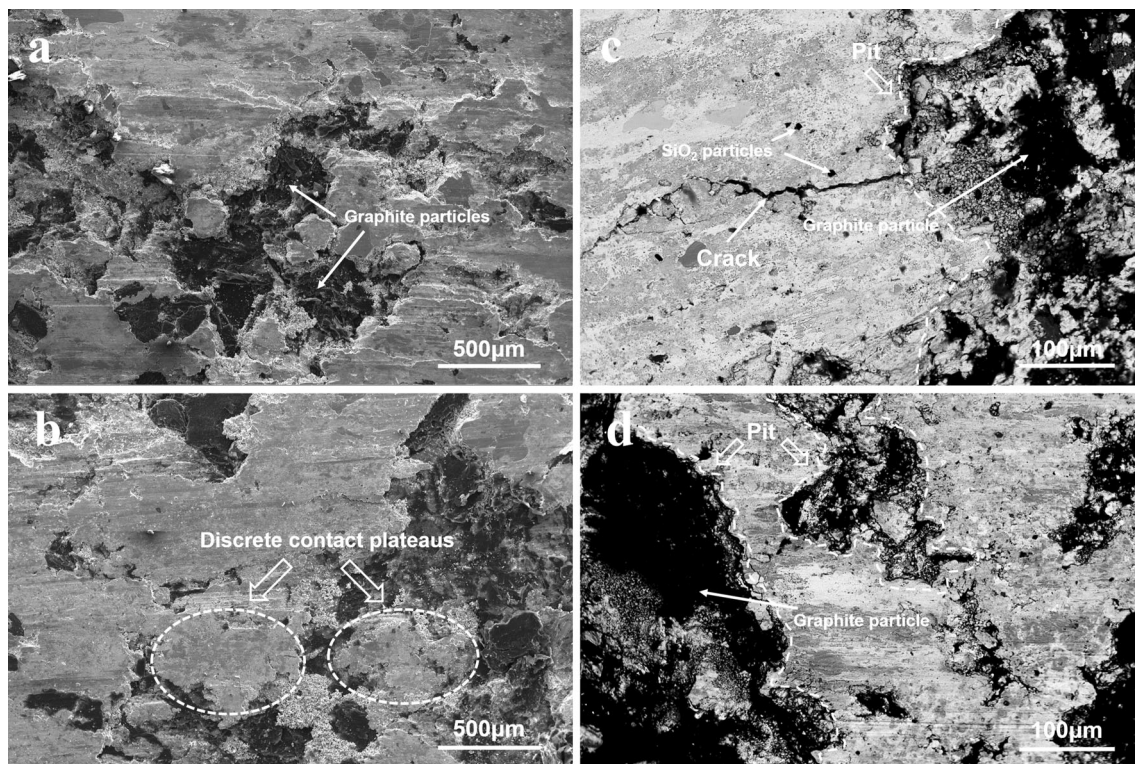
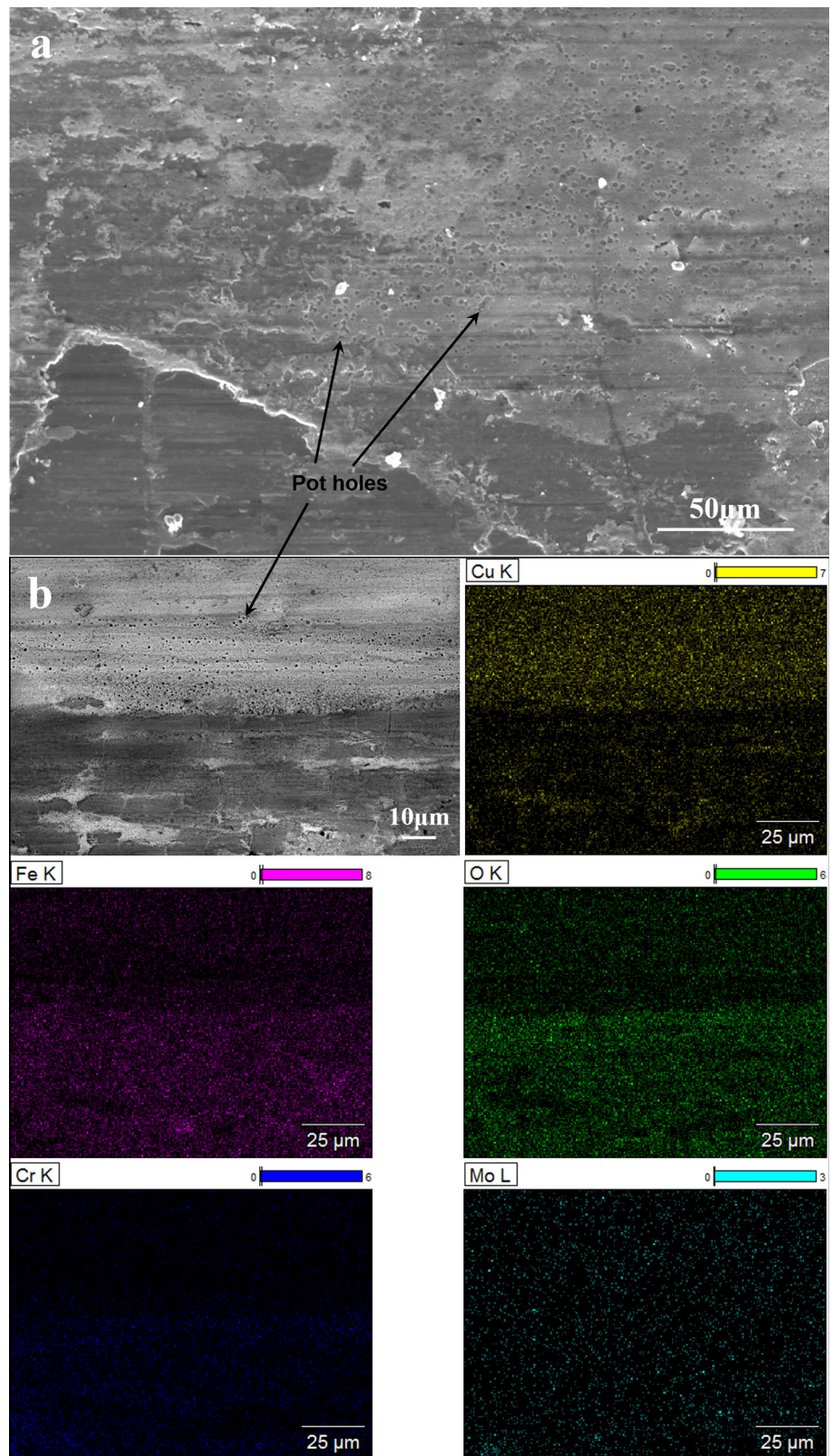


Fig. 8 Surface morphologies at the high-speed stage. SE images: **a** 350 km/h, **b** 380 km/h; BSE images: **c** 350 km/h, **d** 380 km/h

Fig. 9 Friction surface at 380 km/h. **a** Molten holes phenomenon, **b** BSE image and element area profile



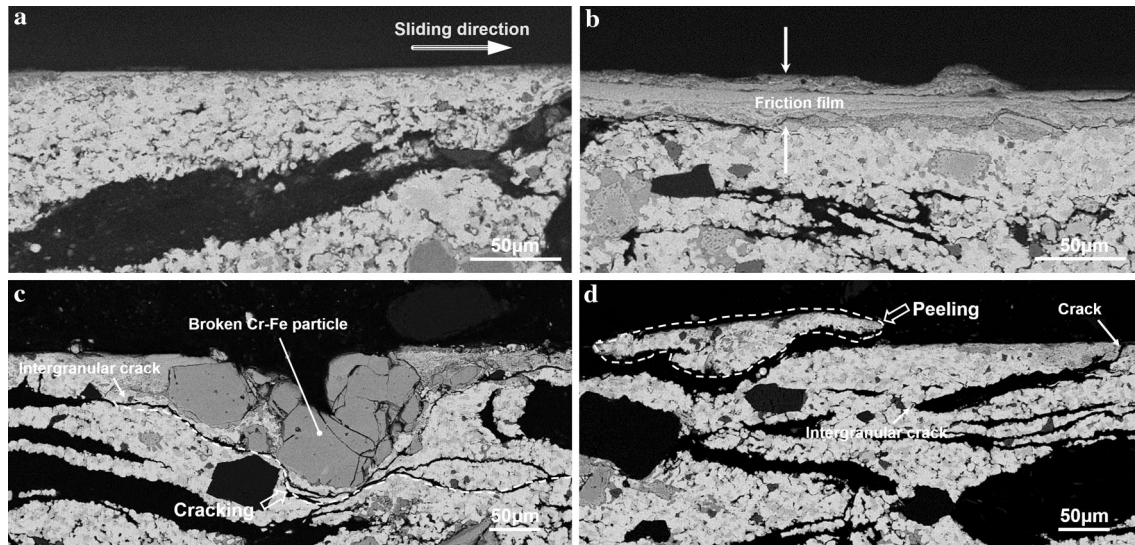


Fig. 10 Representative vertical section microstructures at different IBS. **a** 80 km/h, **b** 200 km/h, **c** 320 km/h, **d** 380 km/h

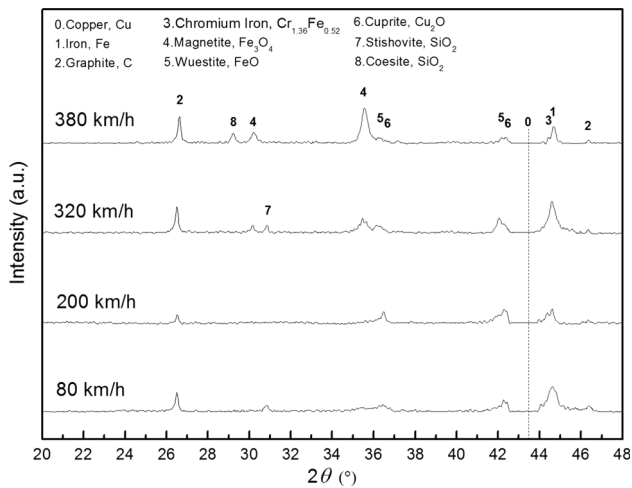


Fig. 11 Representative XRD patterns of the friction surfaces. Cu peak (marked “0”) is too intensive and have been “cut off” from the patterns to allow “raising” the intensity of weaker peaks, and the intensively Cu peak may be attributed to the penetration of friction film by X-ray

be used to explain the decrease in T_{\max} from 626 to 610 °C as IBS increased from 350 to 380 km/h (Fig. 4).

3.3 Wear Behaviors

Figure 12 demonstrates the curves of wear rates versus IBS. According to previous literature and the Chinese mechanical standard, demarcations between wear regimes are identified by the sudden change in wear rates of one order of magnitude under different speeds [22–25]. Thus, three wear regimes are determined by two dividing lines marked at the value of 10^{-5} and 10^{-4} mm³/J in present work (Fig. 12). Specifically, when IBS was less than

200 km/h, the wear rates were nearly a constant of 10^{-5} mm³/J, which could be considered as a mild wear regime. At 200–250 km/h, the wear rates increased and displayed a moderate wear regime. As IBS exceeded 250 km/h, the wear rates surpassed 10^{-4} mm³/J and presented a severe wear regime. It showed a sharply increase until 350 km/h and slackened at 380 km/h.

As described in Sect. 3.2, when IBS was less than 200 km/h, the pad surface was gradually covered by a complete friction film. It is this protective film that contributes to the mild wear regime in this speed range. Meanwhile, we found two types of wear debris below 200 km/h, i.e., the small granular particles and the strip-shaped particles (Fig. 13a). It means that the abrasion and plowing are dominated at this stage. As IBS reached 200 km/h, tribo-oxidation became intensive, which makes it easy for the formed brittle oxide layer to detach from the contact surface (Fig. 5h), and the moderate wear regime was attained. Therefore, abrasive, plough, and oxidative wear are the key wear mechanisms when IBS is no more than 250 km/h.

As IBS exceeded 250 km/h, friction surface displayed a typical feature of delamination (Figs. 6, 8), which may be induced by the cyclic stress under the turbulent motion. With the increase in IBS, the accumulation of plastic deformation caused by the shear and normal stress in the subsurface will eventually lead to the initiation of cracks and delamination. Since the stresses are discontinuously distributed at the interfaces, the weakest interface, i.e., the graphite/matrix interface in the composite, may preferentially act as the stress concentration zone and further develop into the source of the delamination fracture (Fig. 8). The large sheet-like wear debris as well as some

Fig. 12 Wear rates versus IBS for metallic braking pad

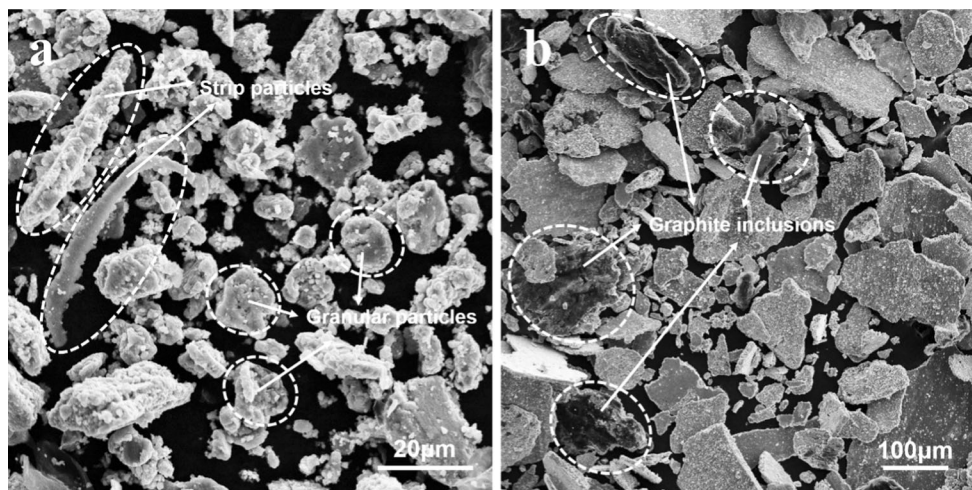
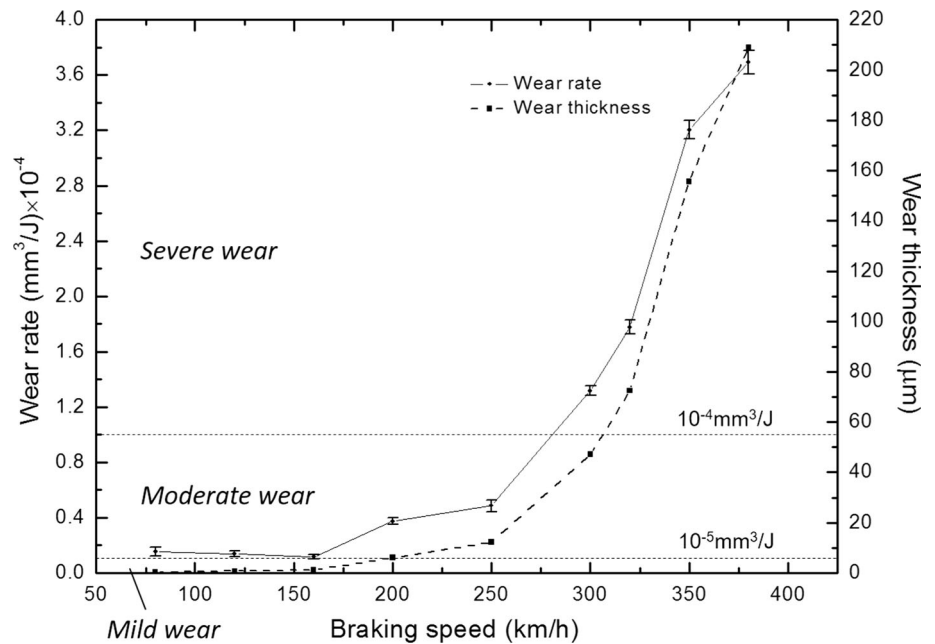


Fig. 13 Wear debris under different IBS. **a** 160 km/h, **b** 350 km/h

graphite inclusions observed at 350 km/h (Fig. 13b), provide evidence to confirm above inferences. Therefore, when IBS exceeded 250 km/h, the predominant wear mechanism is delamination. In addition, the lubricative fluid film may be responsible for the mitigatory wear rate from 350 to 380 km/h.

From the above-mentioned description, the friction and wear behaviors as well as the corresponding characteristics of friction film can be summarized as follows (Table 5). The friction film experienced a formation–completion–destruction process, while the additive particles, like graphite, Cr–Fe, and SiO_2 , experienced an exposure–coverage–exposure process as IBS increased. Consequently, the COFs went through a decline–rise–decline process with the increase in

IBS. On the other hand, it is not until the friction film was ruptured a lot that the severe wear regime occurred.

4 Conclusions

1. The COF of braking pad presented a three-stage feature with the increasing IBS. At the low-speed stage (80–200 km/h), the COF decreased from 0.395 to 0.358 with the increase in IBS. At the medium-speed stage (250–320 km/h), the COF increased to reach a maximum value of 0.398 at 320 km/h. At the high-speed stage (350–380 km/h), it fell to 0.379 with increasing IBS. The fluctuation of the COFs at

Table 5 Summary of all the friction and wear behaviors and characteristics of friction film

IBS (km/h)	Friction behaviors	Characteristics of friction film	Wear behaviors	Wear mechanisms
80	Low-speed stage COF decreased from 0.395 to 0.358	A few patchy friction film Many exposed graphite, powdery and abrasive third body	Mild wear $W_r \approx 10^{-5} \text{ mm}^3/\text{J}$	Abrasion, plowing and oxidation
120		Continuous friction film Buried graphite and hard particles		
160		Complete friction film Buried graphite and hard particles		
200		Complete friction film A pieces of recompacted friction film	Moderate wear $10^{-5} \text{ mm}^3/\text{J}$	
250	Medium-speed stage COF increased from 0.369 to 0.398	Slightly ruptured friction film Some pits and exposed metallic surface	$J < W_r < 10^{-4} \text{ mm}^3/\text{J}$	
300		Ruptured friction film Some pits, exposed Cr–Fe particles and metallic surface	Severe wear $W_r > 10^{-4} \text{ mm}^3/\text{J}$	Delamination
320		Severely ruptured friction film Many pits, crushed Cr–Fe particles, extensive metallic surface		
350	High-speed stage COF decreased from 0.395 to 0.379	Ruined and discrete friction film Many pits, exposed graphite and SiO ₂ particles, cracks		
380		Ruined and discrete friction film Many pits, exposed graphite and SiO ₂ particles, cracks, as well as numerous molten holes		

different IBS is less than 15%, which meet the requirements of CRCC.

- The evolution of the COF has a close relationship with the change of friction film. At the low-speed stage, the friction film gradually covered on the pad surface with the increasing IBS, contributing to a decrease in the COF. At the medium-speed stage, the increase in the COF was attributed to the enhanced “metal-on-metal” contact as well as the exposed Cr–Fe fragments cursed by the removal of friction film. At the high-speed stage, the COF decreased due to the less contact plateau or the melting lubricative film induced by high temperature.
- As IBS increased, the pad displayed three wear regimes, i.e., (i) mild wear (80–160 km/h), (ii) moderate wear (200–250 km/h), and (iii) severe wear (300–380 km/h). The wear rates of the pad were nearly a constant of $10^{-5} \text{ mm}^3/\text{J}$ below 200 km/h, followed by a slow growth until 250 km/h. As IBS exceeded 250 km/h, it showed a sharply increase until 350 km/h and slackened at 380 km/h.
- The dominant wear mechanisms of metallic pad are abrasive, plough, and oxidative wear below 250 km/h, and then they transform into delamination. In addition,

the wear was mitigated by melting lubricative film at 380 km/h.

Acknowledgements Financial support from the National Natural Science Foundation of China under Contract No. 51572026 and No. U1134202 is gratefully acknowledged.

References

- Verma, P.C., Menapace, L., Bonfanti, A.: Braking pad-disc system: wear mechanisms and formation of wear fragments. *Wear* **322**, 251 (2015)
- EL-Tayeb, N.S.M., Liew, K.W.: On the dry and wet sliding performance of potentially new frictional brake pad materials for automotive industry. *Wear* **266**, 275 (2009)
- Kim, Y.C., Cho, M.H., Kim, S.J., Jang, H.: The effect of phenolic resin, potassium titanate, and CNSL on the tribological properties of brake friction materials. *Wear* **264**, 204 (2008)
- Su, L., Gao, F., Han, X., Fu, R., Zhang, E.: Tribological behavior of copper-graphite powder third body on copper-based friction materials. *Tribol. Lett.* **60**, 30 (2015)
- Chan, D., Stachowiak, W.G.: Review of automotive brake friction materials. *Proc Inst Mech Eng D J Automob Eng* **218**, 953 (2004)
- Renz, R., Seifert, G., Krenkel, W.: Integration of CMC brake disks in automotive brake systems. *Int. J Appl. Ceram. Tec.* **9**, 712 (2012)

7. Xiao, P., Li, Z., Xiong, X.: Microstructure and tribological properties of 3D needle-punched C/C-SiC brake composites. *Solid State Sci.* **12**, 617 (2010)
8. Li, G., Yan, Q., Jian, X., Qi, G., Yang, X.: The stability of the coefficient of friction and wear behavior of C/C-SiC. *Tribol. Lett.* **58**, 1 (2015)
9. Krenkel, W., Heidenreich, B., Renz, R.: C/C-SiC composites for advanced friction systems. *Adv. Eng. Mater.* **4**, 427 (2002)
10. Li, G., Yan, Q.: Comparison of friction and wear behavior between C/C, C/C-SiC and metallic composite materials. *Tribol. Lett.* **60**, 15 (2015)
11. Cai, Y., Yin, X., Fan, S., Zhang, L., Cheng, L., Wang, Y., Yin, H.: Effects of particle sizes and contents of ceramic fillers on tribological behavior of 3D C/C composites. *Ceram. Int.* **40**, 14029 (2014)
12. Xiong, X., Chen, J., Yao, P., Li, S., Huang, B.: Friction and wear behaviors and mechanisms of Fe and SiO₂ in Cu-based P/M friction materials. *Wear* **262**, 1182 (2007)
13. Desplanques, Y., Degallaix, G.: Interactions between third-body flows and localisation phenomena during railway high-energy stop braking. *SAE Int. J. Passeng. Cars-Mech. Syst.* **1**, 1267 (2008)
14. Godet, M.: Third-bodies in tribology. *Wear* **136**, 29 (1990)
15. Österle, W., Urban, I.: Third body formation on brake pads and rotors. *Tribol. Int.* **39**, 401 (2006)
16. Desplanques, Y., Degallaix, G.: Genesis of the third-body at the pad-disc interface: case study of sintered metal matrix composite lining material. *SAE Int. J. Mater. Manuf.* **2**, 25 (2009)
17. Sutter, G., Ranc, N.: Flash temperature measurement during dry friction process at high sliding speed. *Wear* **268**, 1237 (2010)
18. Kasem, H., Thevenet, J., Boidin, X., Siroux, M., Dufrenoy, P., Desmet, B., Desplanques, Y.: An emissivity-corrected method for the accurate radiometric measurement of transient surface temperatures during braking. *Tribol. Int.* **43**, 1823 (2010)
19. Wang, Y., Yan, Q., Zhang, F., Ge, C., Zhang, X., Zhao, H.: Sintering behavior of Cr in different atmospheres and its effect on the microstructure and properties of copper-based composite materials. *Int. J. Min. Met. Mater.* **20**, 1208 (2013)
20. Xiao, B., Xing, J., Feng, J., Zhou, C., Li, Y., Su, W., Xie, X., Cheng, Y.: A comparative study of Cr₇C₃, Fe₃C and Fe₂B in cast iron both from ab initio calculations and experiments. *J. Phys. D Appl. Phys.* **42**, 1 (2009)
21. Zhu, Z., Bao, J., Yin, Y., Yin, Y., Chen, G.: Frictional catastrophe behaviors and mechanisms of brake shoe for mine hoisters during repetitious emergency brakings. *Ind. Lubr. Tribol.* **65**, 245 (2013)
22. Gong, T., Yao, P., Xiao, Y., Fan, K., Tan, H., Zhang, Z., Zhao, L., Zhou, H., Deng, M.: Wear map for a copper-based friction clutch material under oil lubrication. *Wear* **328–329**, 270 (2015)
23. Rasool, G., Stack, M.M.: Wear maps for TiC composite based coatings deposited on 303 stainless steel. *Tribol. Int.* **74**, 93 (2014)
24. Chen, J., Lu, N., Peng, S., Ni, X.: Specifications for Sintered Metal Friction Materials JB/T 3063-2011. China Machine Press, China (2012)
25. Riahi, A.R., Alpas, A.T.: Wear map for grey cast iron. *Wear* **255**, 401 (2003)